Substituent Group Variations Directing the Molecular Packing, Electronic Structure, and Aggregation-Induced Emission Property of Isophorone Derivatives

Zheng Zheng, Zhipeng Yu, Mingdi Yang, Feng Jin, Qiong Zhang, Hongping Zhou,* Jieying Wu, and Yupeng Tian

College of Chemistry and Chemical Engineering, Key Laboratory of Functional Inorganic Materials Chemistry of Anhui Province, Anhui University, Hefei, 230039, People's Republic of China

S *Supporting Information*

ABSTRACT: A series of new isophorone derivatives (**1−5**), incorporating the heterocyclic ring or aza-crown-ether group, with large Stokes shifts (>140 nm), have been synthesized and characterized. **1−4** display aggregation-induced emission behaviors, while dye **5** is highly emissive in solution but quenched in the solid state. It was found that the tuning of emission color of the isophorone-based compounds in the solid state could be conveniently accomplished by changing the terminal substituent group. The photophysical properties in solution, aqueous suspension, and crystalline state, along with their relationships, are comparatively investigated.

Crystallographic data of **1−4** indicate that the existence of multiple intermolecular hydrogen bonding interactions between the adjacent molecules restricts the intramolecular vibration and rotation and enables compounds **1−4** to emit intensely in the solid state. The size and growth processes of particles with different water fractions were studied using a scanning electron microscope, indicating that smaller globular nanoparticles in aqueous suspension are in favor of fluorescence emissions. The above results suggest that substituent groups have a great influence on their molecular packing, electronic structure, and aggregation-induced emission properties. In addition, fluorescence cell imaging experiment proved the potential application of **5**.
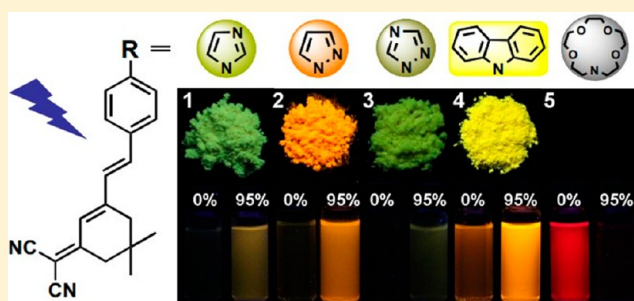
INTRODUCTION

Organic fluorophores exhibiting high nanoaggregation-induced emission and solid- and crystalline-state fluorescence efficiency have received increasing attention owing to their potential applications in fluorescence imaging, light-emitting devices, and active gain media for optically pumped solid-state lasers.[1−4] However, most fluorescent organic materials suffer from the notorious aggregation-caused quenching (ACQ) effect due to strong π−π stacking interactions in extended π-conjugated systems and dipole−dipole interactions in D−A charge transfer systems, which is a typical problem of common organic chromophores and thus limited their applications in real world, which requires materials to be solid and phragmoid films.[5]

Up to now, a variety of conjugated molecules with twisted skeleton conformation have been demonstrated to exhibit aggregation-induced emission (AIE)[6,7] since the first report by Tang and colleagues in 2001.[8] AIE materials are successfully put into application in the construction of OLEDs,[9−11] bioimaging systems,[12,13] and chemical sensors.[14−16] However, the working mechanisms of the AIE processes are so complicated that they still remain unclear, although various theories have been advanced to explain the AIE phenomenon, such as planarity and rotatability,[17−20] intramolecular restrictions,[21,22] intermolecular interactions,[23] ACQ-to-AIE transformation, etc.[24] The intramolecular rotation, one of the most influential mechanisms, was researched in depth.[25,26] Lee et al. reported a group of isophorone-based fluorescent materials as red emitters for use in OLEDs.[27] A series of near-infrared solid-state emitters based on isophorone were reported, and all of the crystalline compounds were fluorescent in the solid state. The results showed that the origin of the emission depends on the nature of the substituent groups that influence the crystal packing and trigger the formation of the long chain of emitting aggregates.[28]

In this paper, we report a new family of isophorone-based fluorescent derivtatives (**1−5**) (Figure 1). Structurally, the imidazol, pyrazol, triazol, and carbazol groups have richer π-electron density than the phenyl group. Aza-crown-ether can not only increase the solubility of the molecule but also enhance the extent of electron delocalization and the ability to donate electrons. Incorporation of the heterocyclic ring or aza-crown-ether group with different electron-donating ability is intended to enrich the π-electron density and increase the dimension of π-electron delocalization of the system. The molecules **1−4** show good AIE characteristics and tunable

Figure 1. Molecular structures of **1**−**5**.

Scheme 1. Synthesis of Fluorophores 1−5

yellow or orange emission. We aim to reveal the structure−property relationship and learn how subtle structural change modulates the emission color, solvatochromism, and AIE features of these isophorone derivatives. The spectroscopic properties of the compounds in solution, nanosuspensions, and their crystal structures were investigated to elucidate the mechanism of enhanced emission in the aggregation state.

■ RESULTS AND DISCUSSION

Design and Synthesis. To enrich the AIE research and broaden its practical applications, we designed a series of new AIE luminogens and devised a multistep reaction route for their synthesis (Scheme 1). 4-(1H-Imidazol-1-yl)benzaldehyde **1a**, 4-(1H-pyrazol-1-yl)benzaldehyde **2a**, 4-(1H-1,2,4-triazol-1-yl)-benzaldehyde **3a**, and 4-(carbazol-9-yl)benzaldehyde **4a** were obtained directly from commercial imidazole, pyrazole, triazole, carbazole, and 4-fluorobenzaldehyde, respectively. 4-(1,4,7,10-tetraoxa-13-azacyclopentadecyl)benzaldehyde was obtained

from N,N-disubstituted aniline via a Vilsmeier−Haack reaction with phosphorus oxychloride and dry DMF. Isophorone, malononitrile, triethyene glycol, and 2,2′-(phenylimino)-diethanol were available commercially. Compounds **1**−**5** can be easily synthesized starting from isophorone, malononitrile, and the corresponding 4-substituted benzaldehyde by a double Knoevenagel reaction sequence, which is easier than the original procedure described by Lemke in 1974,[31] by using dry acetonitrile instead of DMF and only piperidine as a catalyst for the second Knoevenagel condensation.

All intermediates and final products were carefully purified and fully characterized by IR, NMR, and mass spectroscopies, which confirmed their expected molecular structures. Single crystals of compounds **1**−**4** were slowly prepared by a simple vapor diffusion method from the chloroform−methanol system at room temperature and were characterized crystallographically. Their ORTEP drawings are shown in Figures 9a−12a, while Table 2 summarizes the crystal data. All of the
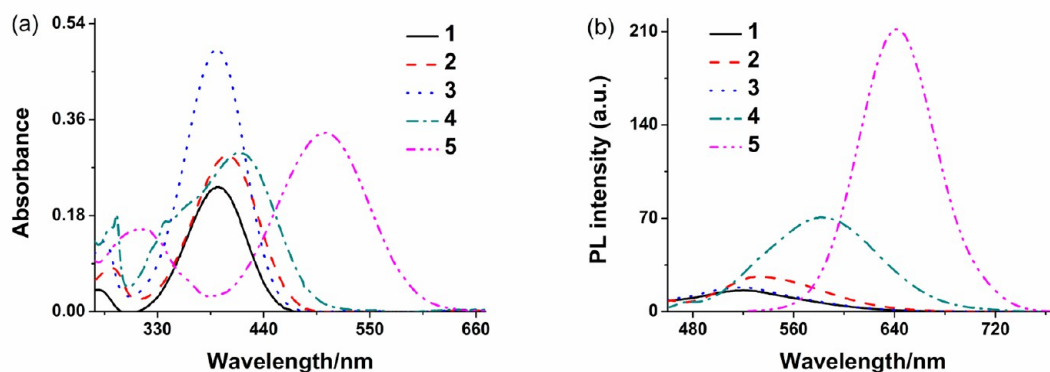
Figure 2. Absorption (a) and PL (b) spectra with the excitation wavelength of 391, 404, 392, 414, and 504 nm for **1–5**, respectively, in ethanol with a concentration of 1×10^{-5} mol L^{-1}.
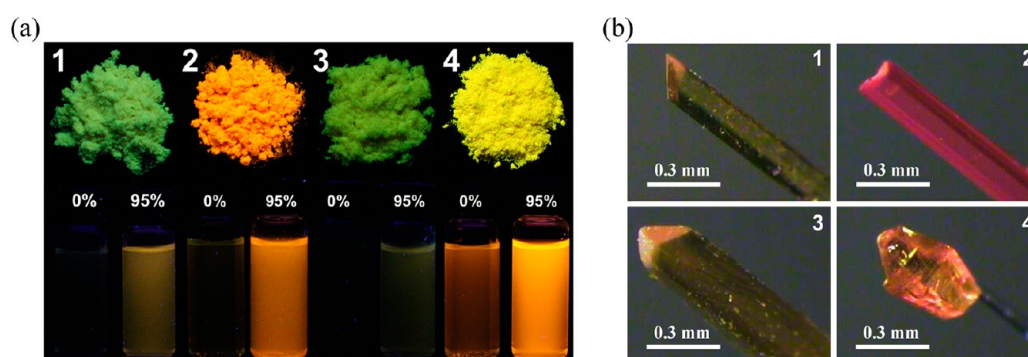

Figure 3. (a) Fluorescent images of **1–4** in ethanol (5×10^{-5} M), ethanol/water (5/95, v/v), and in the form of powder upon excitation with a 365 nm light source. (b) Crystal photographs of **1–4**.

luminogens were soluble in common organic solvents, such as ethanol, tetrahydrofuran (THF), toluene, dichloromethane (DCM), and chloroform, but were insoluble in water.

Photophysical Properties. Upon increasing the solvent polarity, as shown in Supporting Information Table S1 and Figure S1, the fluorescence maxima and the Stokes shift of **1–5** both show monotonically increasing tendency, especially for **4** and **5**. The Stokes shift of **5** increases from 96 nm in benzene up to 147 nm in polar solvent, and the behaviors of **1–4** are similar to that of **5**. This can be explained by the fact that the excited state may possess a higher polarity than that of the ground state, for the solvatochromism is associated with lowering energy level. An increasing dipole–dipole interaction between the solute and solvent leads to a lowering of the energy level, which suggests that compounds **4** and **5** are typical D-π-A chromophores compared with **1–3**. The absorption and photoluminescence (PL) spectra of **1–5** in ethanol at a concentration $c = 1 \times 10^{-5}$ mol L^{-1} are shown in Figure 2. One can see that the absorption spectra exhibits two peaks between 250 and 700 nm, where the low-energy band originates from ICT transition, while the high-energy band is assigned to the π–π* transitions.[32] This series of compounds show their absorption maximum with the following order: **5** (504 nm) > **4** (414 nm) > **2** (404 nm) > **3** (392 nm) ≈ **1** (391 nm). In general, the extension of the π-systems and the strong electron-donating ability exerts an important influence on the absorption spectra. For example, the absorption maximum of **4** at 414 nm is red-shifted by 10–23 nm relative to that of **1**, **2**, and **3**, as **4** containing a carbazole moiety has a larger conjugation length than **1**, **2**, or **3**; the absorption maximum of **5** at 504 nm is red-

shifted by 90–113 nm compared with that of **1**, **2**, **3**, and **4**, which can be ascribed to the stronger electron-donating group of aza-crown-ether of **5** (Figure 2a). As shown in Figure 2b, **1–5** show an emission maximum at 520, 532, 518, 583, and 641 nm, respectively. The ethanol solutions of **4** and **5** emit weak yellow and strong red light, respectively, while **1**, **2**, and **3** are hardly emissive (Figure 3). All of the above information suggests that both absorption and photoluminescence (PL) spectra are in agreement with the order of the extension of the π-systems and the increase of electron-donating ability of the donors: aza-crown-ether > carbazole > heterocyclic ring.

Aggregation-Induced Enhanced Emission. To investigate the AIE attributes of **1–5**, we added different amounts of water, a poor solvent for the luminogens, to the pure ethanol solutions by defining the water fractions (f_w) of 0–95% and then monitored the absorption and PL change with the excitation wavelengths of 391, 404, 392, 414, and 504 nm for **1–5**, respectively.

Figure 4a2 shows that the PL intensity of **1** increases slowly in aqueous mixtures when $f_w < 80\%$ and increases dramatically when $f_w > 80\%$. From the pure ethanol solution to an ethanol–water mixture with $f_w = 95\%$, the PL intensities increase by 9-fold for **1**. Similar enhancement can be observed in the behaviors of **2** and **3**. The PL intensity of **2** enhances 7-fold when f_w increases from 0 to 60%, while the intensity of **3** enhances 11-fold when f_w increases from 0 to 80% (Figure 4b2, c2). The behaviors of **4** are totally different from that of **1–3**. With a gradual addition of water into the ethanol, the emission of **4** is dramatically weakened and the emission color is bathochromically shifted when $f_w \leq 40\%$. The light emission is
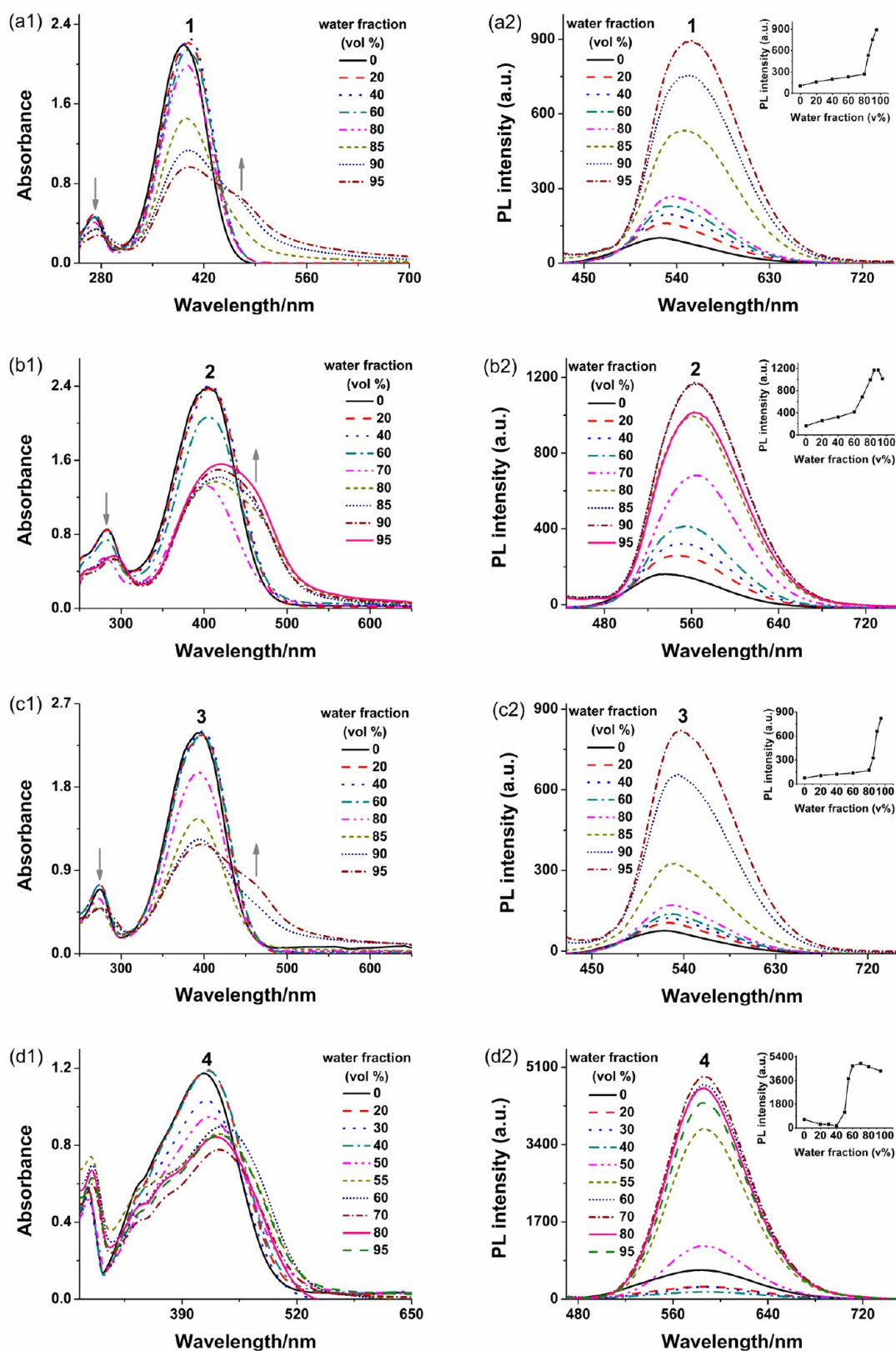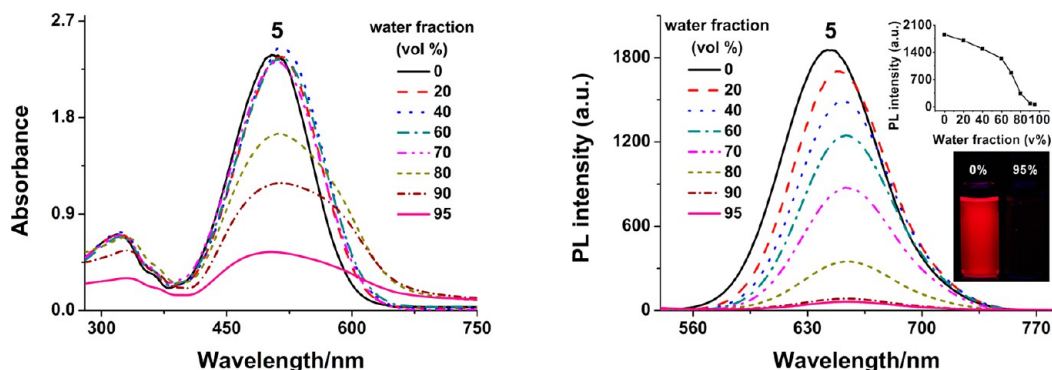
Figure 4. Absorption and PL spectra of **1**−**4** in ethanol/water mixtures with different water fraction (f_w). The inset depicts the changes of PL peak intensity with different water fractions.

invigorated from $f_w \approx 50$ vol % and reaches its maximum value at 70% water content, which is 8-fold higher than that in pure ethanol solution. Meanwhile, the emission maximum was gradually red-shifted to 589 nm when f_w reaches 95 vol %. Moreover, considering that the ethanol solution of **4** emits weak yellow light while **1**−**3** are hardly emissive (Figure 3), **4**

Figure 5. Absorption and PL spectra of **5** in ethanol/water mixtures with different water fraction (f_w). The inset depicts the change of PL peak intensity with different water fraction.

shows a larger torsion angle between the phenyl ring and heterocyclic ring than those of **1−3** in the gas phase or in the crystal because of the large internal steric hindrance, as shown in Figure 8.

It is presumable that in the mixtures with low water fractions (0 to 40%), molecules of **4** may cluster together to form random, amorphous aggregates. When the water fraction becomes high, its molecules may agglomerate in an ordered fashion to form crystallike aggregates.[33] This phenomenon is also probably caused by the change of solvent polarity with addition of water at low water fractions, then the water can interact with solute molecules immediately, which would weaken the emission gradually.[34] As can be seen in Figure 4b2,d2, after reaching a maximum intensity at 90% water content for **2** and 70% water content for **4**, respectively, the PL intensity of the two compounds decreases with increasing water content. This phenomenon was often observed in some compounds with AIE properties, but the reasons remain unclear.[35,36] There are two possible explanations for this phenomenon: (1) After the aggregation, only the molecules on the surface of the nanoparticles emit light and contribute to the fluorescent intensity upon excitation, leading to a decrease in fluorescent intensity. However, the restriction of intramolecular rotations of the heterocyclic rings around the carbon−carbon single bonds in the aggregation state can enhance light emission. The net outcome of these antagonistic processes depends on which process plays a predominant role in affecting the fluorescent behavior of the aggregated molecules.[37] (2) When water is added, the solute molecules can aggregate into two kinds of nanoparticle suspensions: crystal particles and amorphous particles. The former one results in an enhancement in the PL intensity, while the latter leads to a reduction in intensity.[38] Different from **1−4**, with the addition of water, the emission of **5** is gradually weakened or suffers aggregation-caused quenching (ACQ) (Figure 5), more likely due to the aggregation and the presence of excitons presenting parallel transition dipole, which was observed for isophorone derivatives by Massin.[28]

The changes of the integral under emission bands with different water fractions (f_w) were analyzed, which is in line with the changes of PL peak intensity with water fraction (Supporting Information Figure S3). The emission trends of **1−5** remain the same as changing the excitation wavelength to 470 nm for **1−4** and 590 nm for **5** (Figure S4) is probably due to the nanoparticles being composed of molecules that have emissive ability, and the emission trend may depend on the number of the individual molecules in nanoparticles. Figure 3

shows fluorescence images of **1−4** in the ethanol solutions, nanoparticle suspensions (95% water content), and powder under UV light. In a word, these increases in fluorescence intensity of **1−4** were considered to be a result of the AIE effect. As aggregates formed, the restriction of intermolecular rotation increased, which led to increased fluorescence emission. The notorious effect of ACQ of **5** indicates that the AIE effect of the compounds is dominated by substitution.

The absorption spectra of compounds **1−4** in the ethanol/water mixtures (50 μM) are shown in Figure 4a1−d1. The spectral profiles of **1**, **2**, and **3** are significantly changed when f_w > 85, 80, and 90%, respectively. Meanwhile, the absorption peaked at 400 nm, with a shoulder around 460 nm emerging initially. The intensities of absorption peaks of the compounds **1−3** positioned at 270 and 400 nm gradually decrease with the increasing water content, while the shoulder peak located at ∼460 nm emerges afterward and then gradually becomes strong, indicating the formation of nanoscopic aggregates of the compounds **1−3**. **4** exhibits the same behaviors as **1−3**, with the increasing water fractions, the corresponding intensities of the peaks gradually decrease and the maximum absorption wavelength gradually red shifts. The light scattering, or Mie effect, of the nanoaggregate suspensions in the solvent mixtures effectively decreases light transmission in the mixture and causes the apparent high absorbance and level-off tail in the visible region of the UV absorption spectrum.[39,40]

The growth progresses of **1** and **2** were studied by scanning electron microscopy (SEM) with different water fractions. For **1**, upon injection of ethanol into the mixture of ethanol/water (40/60, v/v), nanoaggregates formed immediately with sizes varying from 150 to 250 nm. Much smaller globular nanoparticles with a size range of 50−150 nm were obtained in ethanol/water (5/95, v/v) (Figure 6a,b). The diameter of the nanoparticles decreases with the increasing proportion of water owing to the more compact aggregation, which is also verified by the SEM images for **2** (Figure 6c,d). This phenomenon suggests that the diameters of the nanoparticles are correlated with the ethanol/water ratio.[41,42] The decreasing diameters of nanoparticles upon increasing amount of water, as shown in SEM images, give us direct evidence of molecular aggregation during the emission enhancement, while smaller globular nanoparticles in ethanol/water (5/95, v/v) are in favor of fluorescence emissions.

To have a quantitative comparison, we measured the fluorescence quantum yields (Φ_F) of the molecules in both the solution and crystal. The experimental errors are estimated to be ±15% from sample concentrations and instruments. The
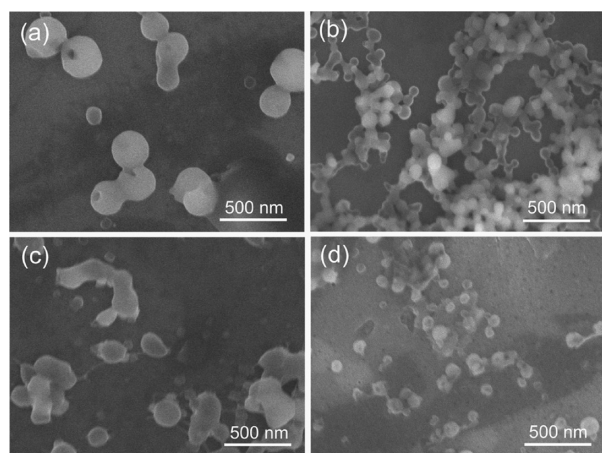
Figure 6. SEM images of **1** and **2** in ethanol/water mixtures at concentrations of 5×10^{-5} M with different water fractions: (a) **1** in ethanol/water (40/60, v/v); (b) **1** in ethanol/water (5/95, v/v); (c) **2** in ethanol/water (40/60, v/v); (d) **2** in ethanol/water (10/90, v/v).

Φ_F values of **1−4** in the solid state are 2.7, 12.9, 3.8, and 16.6%, respectively, measured by using an integrating sphere, which are higher than that of **1−4** in the solution ($\Phi_F < 0.1\%$ for **1−3**, $\Phi_F = 0.5\%$ for **4**) and manifest their AIE feature (Table 1). On the contrary, the Φ_F value of **5** solid is <0.1%, which is much lower than that of its ethanol solution ($\Phi_F = 11.1\%$). The changes of the fluorescence quantum yield (Φ_F) from solution to crystal also confirm the opposite aggregation-induced fluorescence behaviors of **1−4** and **5** (Table 1). The substitution group varying from heterocycle or carbazole to aza-crown-ether produces a significant increase in the solution fluorescence efficiency and the obvious reduction in the solid fluorescence efficiency. Therefore, the opposite aggregation-induced fluorescence behaviors of **1−4** and **5** may be mainly attributed to the difference of the substitution group.

Time-resolved fluorescence measurements were performed and the detailed data of the fluorescence decay curves of **1−5** are listed in Table 1 (Figure S2). The experimental errors are estimated to be ±11% from sample concentrations and instruments. The lifetime of **1−5** in ethanol is obtained by monitoring at the monomer emission. The decay behavior of **1−5** is in a double-exponential manner in the solution obtained by monitoring at the monomer emission. The lifetime of **1−4** is almost from the contribution of the shorter lifetime species, while the lifetime of **5** is mainly from the contribution of longer

lifetime species. As shown in Table 1, the weighted mean lifetime of **5** (0.79 ns) in ethanol is much longer than that of **1** (0.03 ns), **2** (0.05 ns), **3** (0.05 ns), and **4** (0.12 ns). This may be attributed to the larger delocalization of the lone pair of electrons on the N atom from **5**, leading to a larger molecular stabilization effect for the excited state of the aza-crown-ether group.[43] Moreover, the solid of **1**, **2**, and **4** decays through three main relaxation pathways, while the decay behavior of **3** can be fitted with a double-exponential behavior, which all show obviously longer weighted mean lifetimes compared to the pure solvents when monitoring at 370 nm. The long lifetime indicates the existence of new aggregation species or excitonic couplings. The decay of the powder of **5** is too fast to be measured with our equipment (the limit is 0.01 ns).

Additionally, the fluorescence lifetimes of **5** in solution were calculated by multiplying the corresponding quantum yield on natural lifetime, which can be easily calculated from the known Strickler−Berg equation (eq 1).[44] A calculated fluorescence lifetime of 0.72 ns was obtained, which is in excellent agreement with the experimental value (0.79 ns) and further validates the experimental time-resolved technique.

$$\frac{1}{\tau_0} = 2.88 \times 10^{-9} n^2 \frac{\int I(\tilde{v}) d\tilde{v}}{\int I(\tilde{v}) \tilde{v}^{-3} d\tilde{v}} \int \frac{\varepsilon(\tilde{v})}{\tilde{v}} d\tilde{v} \tag{1}$$

in which n is the refractive index, I is the fluorescence emission, ε is the extinction coefficient, and $\tilde{v}$ is the wavenumber.

The natural radiative lifetime τ_0 and the fluorescence lifetime τ are related through the quantum yield Φ by

$$\Phi = \frac{\tau}{\tau_0} \tag{2}$$

Different Properties at the Different States. To gain further insight into the AIE mechanism of **1−4**, we conducted a series of absorption and PL measurements in the pure solutions, the mixed solutions with $f_w = 95\%$, the powder, and the single crystals (Figure 7). The crystalline-state geometries were obtained directly from single-crystal data. The geometries in the gas phase of **1−4** (generally, the molecular geometry in the dilute solution can be represented with that of the gas phase) were obtained by geometry optimization in vacuum, which was based on their crystallographic data for quantum-chemical modeling. Figure 7a1−d1 show absorption spectra of the different states of **1−4** grounded in barium sulfate. All spectra are considerably broadened and red-shifted compared to the solution. Emission spectra were

Table 1. Fluorescence Quantum Yield and Fluorescence Lifetime of 1−4 in Ethanol Solution and Solid

sample	λ_{det}[c] (nm)	τ_1[d] (ns)	A_1[e]	τ_2[d] (ns)	A_2[e]	τ_3[d] (ns)	A_3[e]	$\langle \tau \rangle$[f] (ns)	χ^2	Φ_F[g]
1-solution[a]	530	0.03	1.00	5.27	0.00			0.03	1.21	<0.1%
1-solid[a]	523	0.10	0.90	0.58	0.10	4.25	0.00	0.15	1.15	2.7%
2-solution[a]	528	0.05	1.00	5.92	0.00			0.05	1.21	<0.1%
2-solid[a]	579	0.18	0.96	1.18	0.04	4.15	0.00	0.22	1.07	12.9%
3-solution[a]	532	0.05	1.00	4.69	0.00			0.05	1.32	<0.1%
3-solid[a]	530	0.27	0.98	1.21	0.02			0.29	1.25	3.8%
4-solution[a]	579	0.12	1.00	3.72	0.00			0.12	1.31	0.5%
4-solid[a]	553	0.36	0.64	1.64	0.34	6.62	0.01	0.85	1.12	16.6%
5-solution[b]	648	0.43	0.25	0.90	0.75			0.79	1.23	11.1%
5-solid[b]	648	<0.01						<0.01		<0.1%

[a]$\lambda_{ex} = 370$ nm. [b]$\lambda_{ex} = 460$ nm. [c]Detection wavelength. [d]Fluorescence lifetime. [e]Fractional contribution. [f]Weighted mean lifetime. [g]Fluorescence quantum yield measured by using an integrating sphere.
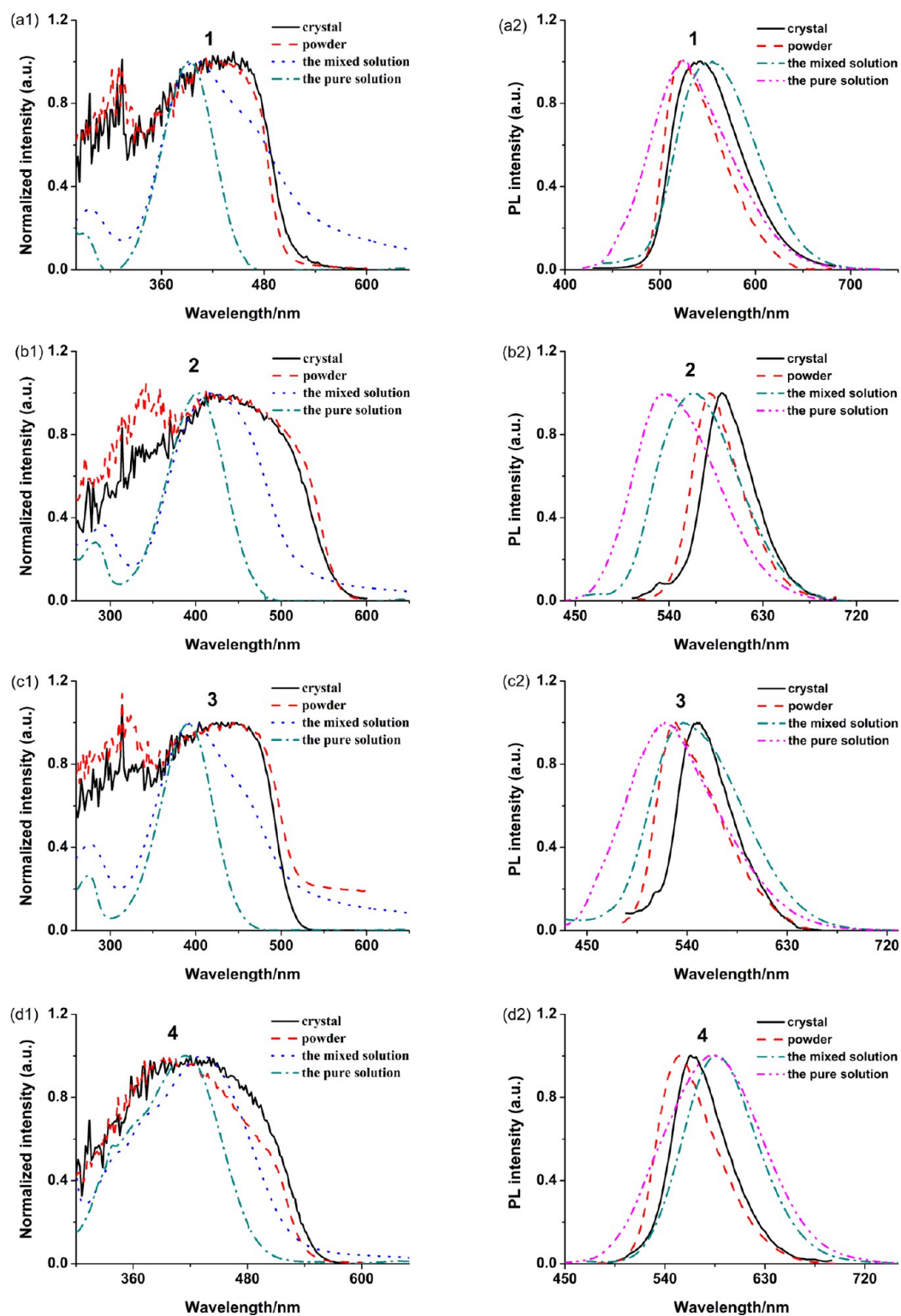
Figure 7. Absorption and PL spectra in the pure solvent, the mixed solution with $f_w = 0.95$, the powder, and the crystal.

recorded with an excitation wavelength at 391, 404, 392, and 414 nm for **1–4**, respectively, close to the absorption maximum found in barium sulfate. Only one structureless emission peak was observed whatever the compound. Figure 7b2,c2 shows that the λ_{em} values of **2** and **3** exhibit the minimum values in ethanol and the maximum values in the form of crystal. The crystal compound **2** emits a strong orange-red fluorescence with the peak wavelength of 590 nm, while **3** emits a strong

yellow fluorescence with the peak positioned at 550 nm (Figure 3). They are obviously red-shifted 58 and 32 nm, respectively, with respect to the values of 532 nm for **2** and 518 nm for **3** in ethanol solution. Figure 8 shows that the optimized geometries of both **2** and **3** molecules in the gas phase have twisted conformation with a larger torsion angle of 13.34 and 17.32° between the phenyl ring and heterocycle than those of the crystal state (6.57 and 7.66°) (Figure 8), respectively, which is
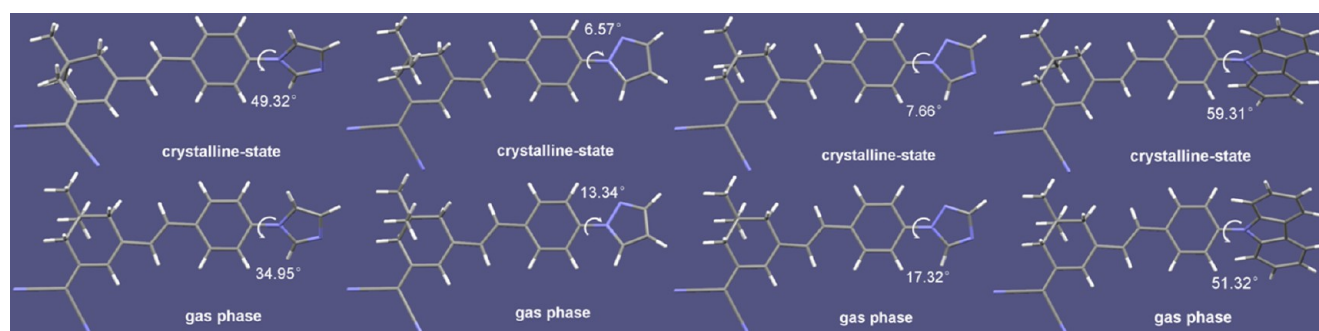
Figure 8. Molecular structures of **1**−**4** in the crystal and in the isolated state.

Table 2. Crystallographic Data for 1−4

compound	1	2	3	4
empirical formula	$C_{22}H_{20}N_4$	$C_{22}H_{20}N_4$	$C_{21}H_{19}N_5$	$C_{31}H_{25}N_3$
formula weight	340.42	340.42	341.41	439.54
crystal system	triclinic	monoclinic	monoclinic	monoclinic
space group	$P\bar{1}$	$P2_1/c$	$P2_1/c$	$P2_1/n$
a [Å]	5.743(5)	6.149(5)	6.439(5)	12.286(5)
b [Å]	9.430(5)	7.323(5)	7.222(5)	13.694(5)
c [Å]	18.057(5)	40.953(5)	39.313(5)	15.580(5)
α [°]	90.784(5)	90.000(5)	90.000(5)	90.000(5)
β [°]	94.855(5)	90.751(5)	90.207(5)	110.838(5)
γ [°]	106.042(5)	90.000(5)	90.000(5)	90.000(5)
V [Å³]	935.7(10)	1844(2)	1828.1(19)	2449.8(16)
Z	2	4	4	4
T [K]	298(2)	298(2)	298(2)	298(2)
D_{calcd} [g·cm⁻³]	1.208	1.226	1.240	1.192
μ [mm⁻¹]	0.073	0.075	0.077	0.070
θ range [°]	1.13−25.00	0.99−25.00	1.04−25.00	1.83−24.99
total no. data	6710	13493	25032	17145
no. unique data	3259	3248	3233	4312
no. params refined	237	237	237	309
R_1	0.0408	0.0475	0.0725	1.014
wR_2	0.1261	0.1290	0.1945	0.0400
GOF	1.021	0.995	1.172	0.1253
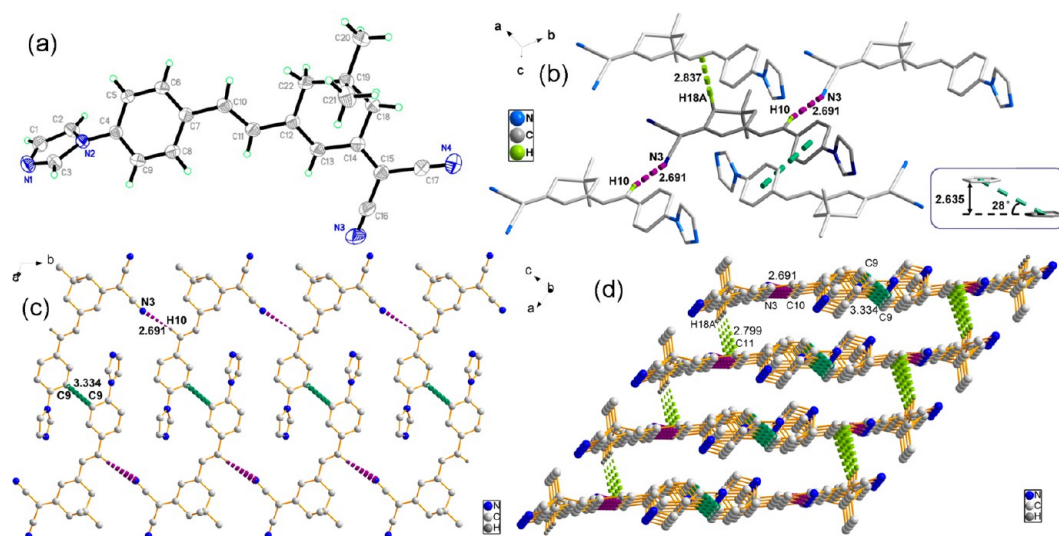
Figure 9. (a) ORTEP diagram of **1**. (b) Restricted twisting motions in crystals of **1**. (c) One-dimensional chain of **1** showing the C−H···N (violet) hydrogen bond and the π−π stacking (sea green) along the *b*-axis. (d) Two-dimensional layer structure of **1** showing the C−H···π stacking (lime) along the *a*-axis. Hydrogen atoms except H10 and H18A are omitted for clarity.
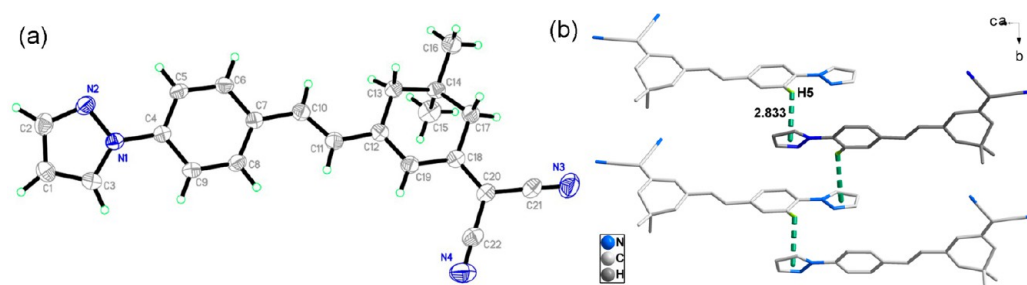
Figure 10. (a) ORTEP diagram of **2**. (b) Restricted twisting motions in crystals of **2**. Hydrogen atoms except H5 are omitted for clarity.
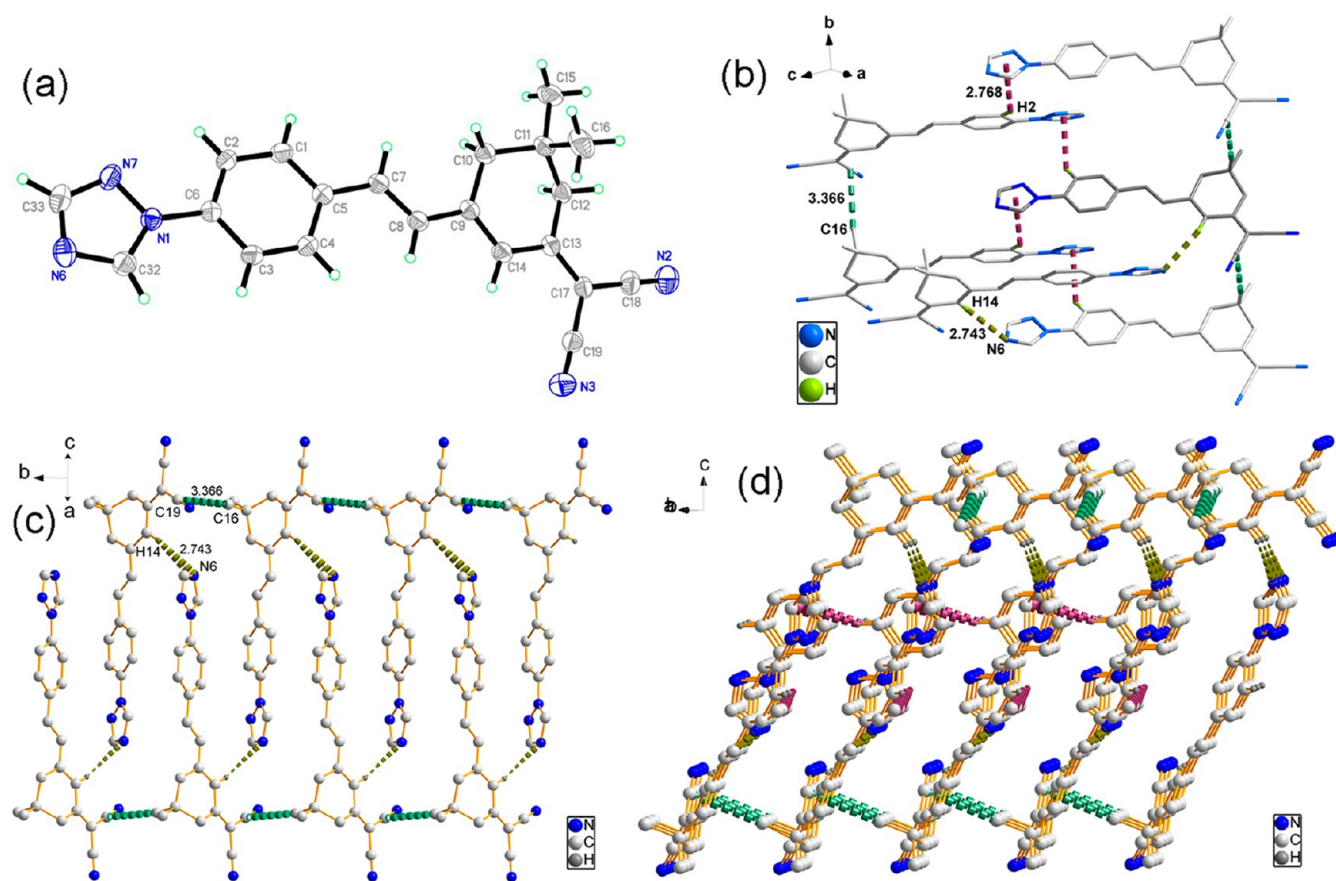

Figure 11. (a) ORTEP diagram of **3**. (b) Restricted twisting motions in crystals of **3**. (c) One-dimensional chain of **3** showing the C−H···N (dark yellow) along the *b*-axis. (d) Two-dimensional layer structure of **3** showing the C−H···π stacking (plum). Hydrogen atoms except H2 and H14 are omitted for clarity.

different from that of **4**. The crystals of **4** emit a yellow fluorescence with the peak wavelength of 565 nm, which is blue-shifted 18 nm compared with that in ethanol (583 nm), which is ascribed to the smaller dihedral angle in ethanol (51.32°) than that of crystal (59.31°), and the less distorted conformations permit effective conjugation and result in red-shifted emission (Figure 7d2). However, the significantly red-shifted emission of **1** in the crystalline state and mixed solution compared with that of ethanol could not be explained by the above-mentioned viewpoint; the reason is still unclear and will be explored further.

Moreover, the emission maxima of the crystals **1** and **4** are about 540 and 565 nm, respectively, which are blue-shifted by 13 and 22 nm compared with those of the mixed solution (553 nm for **1** and 587 nm for **4**), which may be attributable to the conformation twisting of the heterocyclic rings of the

luminogens to fit into the crystalline lattices. Without such restraint, the molecules in the amorphous state may assume a more planar conformation and thus show a redder luminescence.[45] Furthermore, as shown in Figure 8, both **1** and **4** molecules show a larger torsion angle between the phenyl ring and heterocycle than those of **2** and **3** in the gas phase or in the crystal because of the large internal steric hindrance between the two H atoms on imidazol or carbazol and the two H atoms on phenyl.

Mechanisms of Emission Enhancement. The observations of aggregation-induced emission (AIE) triggered us to elucidate the molecular arrangement in crystals. In order to better understand the mechanism, single crystals of **1**, **2**, **3**, and **4** were obtained by slow evaporation from methanol/CHCl₃ mixture solution. Their crystal data and collection parameters are summarized in Table 2.
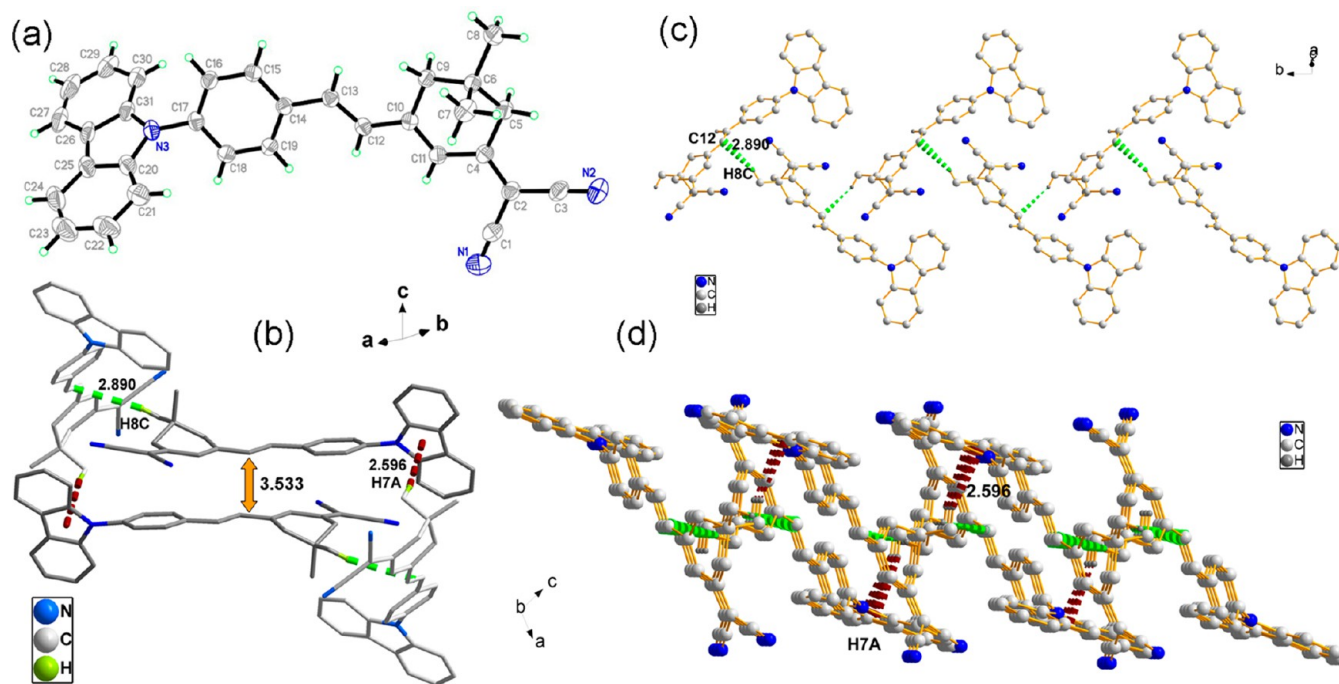
Figure 12. (a) ORTEP diagram of **4**. (b) Restricted twisting motions in crystals of **4**. (c) One-dimensional chain of **4** showing the C−H···π (bright green) along the *b*-axis. (d) Two-dimensional layer structure of **4** showing the C−H···π stacking (dark red). Hydrogen atoms except H8C and H7A are omitted for clarity.

The ORTEP diagrams with atom numbering scheme and some of the interactions in the crystal have been depicted in Figures 9a−12a. The dihedral angles between the heterocyclic ring and the phenyl plane are 49.32° for **1**, 6.57° for **2**, 7.66° for **3**, and 59.31° for **4**. The data of the crystals show that the planarity of both **2** and **3** is better than that of **1** and **4**, which may be due to the large hindrance between the two H atoms on imidazol or carbazol and the two H atoms on phenyl. Figure 9b shows that the flexible molecule **1** is restricted by the C−H···N hydrogen bonds (d = 2.691 Å), C−H···π staking interactions (d = 2.837 Å), and partial π···π staking interactions (a vertical distance of 2.635 Å with an angle of 28°) from the adjacent molecules. As for the phenyl rings slipping along the axis, there is no overlapped phenyl rings, and the shortest C···C distance is 4.064 Å, which could avoid the maximum face-to-face stacking causing the quenched emission (as seen in the inset of Figure 9b). Thus, the photoisomerization process can effectively be prevented. Furthermore, the 1D chain and 2D layer structure of **1** are formed through C−H···N hydrogen bonds, π−π staking interactions, and C−H···π staking interactions (Figure 9c,d). The case of **3** is the same with **1** and is restricted by the C−H···N hydrogen bonds (d = 2.743 Å), C−H···π staking interactions (d = 2.768 Å), and C···π staking interactions (d = 3.366 Å) from the adjacent molecules (Figure 11b). These interactions also form the 1D chain and 2D layer structure shown in Figure 11c,d. In **4**, the molecules are fixed into centrosymmetric antiparallel dimers by the two adjacent molecules, and the distance between them is 3.533 Å (Figure 12b). Figure 12c,d shows its 1D chain and 2D layer structure, respectively. However, completely different from **1**, **3**, and **4**, **2** only exists as a C−H···π interaction as indicated from the packing diagram shown in Figure 10b.

For compounds **1−4**, neither J nor H aggregates could be observed (Figures 9−12). Meanwhile, from further inspection of the crystal structures of **1**, **2**, **3**, and **4**, however, multiple C−H···π hydrogen bonds with distances of 2.596−2.837 Å are formed between the hydrogen atoms of the phenyl rings in one molecule and the π cloud of planar heterocyclic ring in another molecule (Figures 9−12). This is a common feature of AIE active molecules.[46−48] Beside C−H···π interactions, there also exist C−H···N, C···π, and partial π···π interactions within the aggregate structure. The various intermolecular interactions help rigidify the conformation and lock the intramolecular rotations of the heterocyclic ring and the phenyls against the central isophorone unit. As a result, the excited-state energy consumed by intramolecular rotation is greatly reduced, thus enabling the molecules to emit intensely in the solid state.

The molecule packing in the solid state would produce dual roles on the fluorescence.[49] On the one hand, intermolecular interaction could possibly form the species such as excimers and exciplexes, resulting in the quenched emissions. On the other hand, aggregation can restrict the intramolecular motion, intersystem crossing, intramolecular photochemical reactions, etc., which could reduce the nonradiative decay channels and enhance the emission. The competition between these two opposite factors determines the aggregation-induced fluorescence. For the isophorone derivatives, the variations in substitution group bring dramatic changes in the fluorescence in ethanol solvent and the AIE processes in mixed solution. As for the dual roles of molecule packing in the emission, it is obvious that the advantageous side outweighs the disadvantageous one for **1**, **2**, **3**, and **4**. As for **5**, the solution emission is related to the isolated molecule instead of the excimer. The solution emission efficiency is much higher than that of **1**, **2**, **3**, and **4** solution. However, the aggregation process of **5** molecules, in a whole, creates a disadvantageous effect on the emission.

Electronic Structure. To understand the relationship between the optical property and electronic structure, the HOMO and LUMO of **1−5** were calculated by DFT/B3LYP/
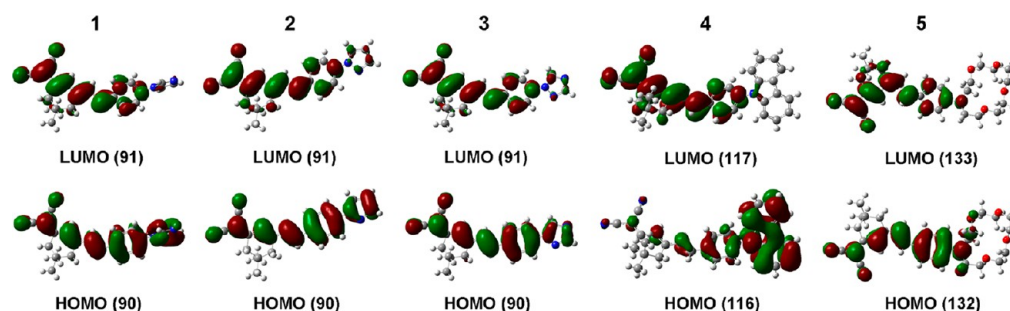
Figure 13. Energy level and electron density distribution of frontier molecular orbitals of dyes 1−5.

6-31G (d) based on the molecule conformation in the crystal structure (Figure 13).[50−52] The results indicate that calculated band gaps of 1−5 are different (3.08, 3.01, 3.18, 2.35, and 2.61 eV for 1−5, respectively), and the values of 4 and 5 are smaller than 1, 2, and 3, which is consistent with the absorption maximum. The results reveal that increasing extension of the π-systems and electron-donating ability of the donors both can lower the band gaps obviously. The theoretical study also nicely explains the bathochromic shift in the absorption and emission of 4 and 5 relative to those of 1, 2, and 3.

Cell Imaging Application of 5. Considering the solubility of the molecule, the chromophore 5 containing aza-crown-ether was picked out due to its high quantum yield and large Stokes shift (147 nm). To evaluate the performance of 5 in living cells, fluorescence microscopy imaging was performed. HepG2 cells were the testing candidates and were cultured and stained with 5. A bright-field image (Figure 14B) of each cell
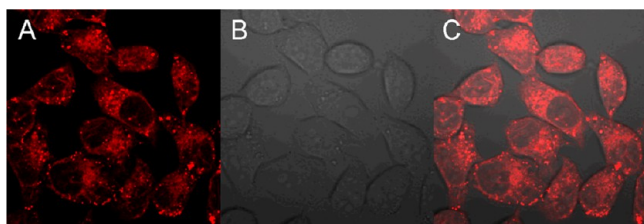

Figure 14. (A) Fluorescent images of HepG2 cells and (B) bright-field image of HepG2 cells stained with 5. (C) Merged image.

was taken immediately prior to the imaging. The fluorescent images and the merged image show that after a 2 h incubation with HepG2 cells (Figure 14A,C), 5 went through the membrane and just localized uniformly in the cytoplasm. The intense fluorescence is mainly because 5 internalizes in the HepG2 cell cytoplasm and the distribution in the nucleolus is significantly lower, suggesting that only the cell cytoplasm can be labeled by 5. These results demonstrate the bioimaging application of 5 by labeling HepG2 cells and also its low toxicity for living cells.

Considering their application in intracellular imaging, the MTT assay was performed to ascertain the cytotoxic effect of 5 against HepG2 cells over a 24 h period. Cytotoxicity is a potential side effect of dyes that must be controlled when dealing with living cells or tissues. Figure 15 shows the cell viability for HepG2 cells treated with 5 at different concentrations for 24 h. The results clearly indicate that HepG2 cells incubated with concentration of 5 μm of 5 remain 90% viable after 24 h of feeding time, demonstrating the superior biocompatibility of 5. Besides, it is found that high concentration only leads to a gradual decrease of viable cells, as
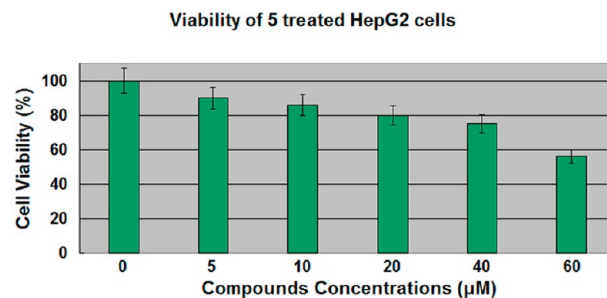

Figure 15. MTT assay of HepG2 cells treated with 5 at different concentrations for 24 h.

shown in Figure 15. As a result, cytotoxicity tests definitely indicate that the low micromolar concentrations of 5 have small toxic effects on living cells over a period of 24 h, and 5 indeed has great potentials for biological studies.

CONCLUSION

In summary, a series of flexibly cored chromospheres 1−5 with different functional terminal groups have been designed and synthesized. All luminogenic molecules show solvatochromism with large Stokes shifts (>130 nm). The compounds 1−4 show weak fluorescence, while 5 shows strong emission in the pure ethanol solution. The PL of the nanoaggregates of 5 in aqueous suspension is quenched by aggregate formation, while that of 1−4 is enhanced, demonstrating a typical AIE phenomenon. Crystallographic data of 1−4 indicate that there is neither J aggregates nor H aggregates observed in the crystal. The existence of multiple C−H···π bonds and C−H···N interactions between the adjacent molecules restricts the intramolecular rotations and blocks the nonradiative processes, resulting in the enhanced emissions. The DFT calculations result in HOMOs and LUMOs consistent with the absorption spectra of the compounds 1−5. The results demonstrate that the structural variation has a great influence on their photophysical properties, molecular packing, electronic structure, and aggregation-induced emission properties. Furthermore, we also demonstrated that 5 can be utilized as fluorescent visualizers for intracellular imaging due to its excellent biocompatibility and low toxicity.

EXPERIMENTAL SECTION

General. All reagents were obtained commercially and used as supplied. The compound 2-(3,5,5-trimethylcyclohex-2-enylidene)-malononitrile was prepared according to the literature.[28] 4-(1H-imidazol-1-yl)benzaldehyde, 4-(1H-pyrazol-1-yl)benzaldehyde, 4-(1H-1,2,4-triazol-1-yl)benzaldehyde, 4-(carbazol-9-yl)benzaldehyde, and 4-(1,4,7,10-tetraoxa-13-azacyclopentadecyl)benzaldehyde were prepared according to literature procedures.[22,29,30] IR spectra were recorded

with a FT-IR spectrometer (KBr discs) in the 4000−400 cm^{-1} region. The NMR spectra were recorded on a 400 MHz NMR instrument using CDCl$_3$ as solvent. Chemical shifts were reported in parts per million (ppm) relative to internal TMS (0 ppm) and coupling constants in hertz. Splitting patterns were described as singlet (s), doublet (d), triplet (t), quartet (q), or multiplet (m). The X-ray diffraction measurements were performed on a CCD area detector using graphite monochromated Mo Kα radiation (λ = 0.71069 Å) at 298(2) K. Intensity data were collected in the variable ω-scan mode. The structures were solved by direct methods and difference Fourier syntheses. The non-hydrogen atoms were refined anisotropically, and hydrogen atoms were introduced geometrically. Calculations were performed with the SHELXTL-97 program package. For time-resolved fluorescence measurements, the fluorescence signals were collimated and focused onto the entrance slit of a monochromator with the output plane equipped with a photomultiplier tube. The decays were analyzed by "least squares". The quality of the exponential fits was evaluated by the goodness of fit (χ^2). The absolute photoluminescence quantum yield (Φ_F) values of the solid and ethanol solution (5 × 10^{-5} M) were determined using an integrating sphere. Crystallographic data (excluding structure factors) for the structure(s) reported in this paper have been deposited with the Cambridge Crystallographic Data Centre as supplementary publication no. CCDC: 916477, 916478, 916479, 916480.

Preparation of 1. Under nitrogen, 4-(1H-imidazol-1-yl)-benzaldehyde (2.4 g, 13.8 mmol) and 2-(3,5,5-trimethylcyclohex-2-enylidene)malononitrile (2.6 g, 13.8 mmol) were dissolved in dry acetonitrile (100 mL). Ten drops of piperidine were added, and the solution was stirred at 40 °C for 8 h. After cooling the reaction mixture, the yellow solid was filtered, washed with acetonitrile, and dried: yield 2.50 g (53%); mp 222 °C; ^{1}H NMR (400 Hz, CD$_3$Cl) δ (ppm) 7.92 (s, 1H), 7.63 (d, 2H), 7.44 (d, 2H), 7.33 (s, 1H), 7.2 (s, 1H), 7.04 (d, J = 16.0 Hz, 1H), 7.02 (d, J = 16.0 Hz, 1H), 6.88 (s, 1H), 2.62 (s, 2H), 2.48 (s, 2H), 1.10 (s, 6H); ^{13}C NMR (100 MHz, CDCl$_3$) δ (ppm) 169.0, 153.1, 137.9, 135.4, 135.0, 134.8, 130.9, 130.0, 129.0, 124.1, 121.5, 117.8, 113.3, 112.6, 79.4, 43.0, 39.2, 32.0, 28.0; IR (KBr, cm^{-1}) 2965, 2925, 2870, 2218, 1608, 1572, 1511, 1455, 1400, 1054, 813; MALDI-TOF calcd for [M + H]$^+$, 341.177; found, 341.179.

Preparation of 2. The orange crystalline solid **2** was prepared according to a similar procedure of **1** using 4-(1H-pyrazol-1-yl)benzaldehyde instead of 4-(1H-imidazol-1-yl)benzaldehyde: yield 3.62 g (77%); mp 243 °C; ^{1}H NMR (400 Hz, CD$_3$Cl) δ (ppm) 7.97 (d, 1H), 7.76−7.74 (t, 3H), 7.61 (d, 2H), 7.09 (d, J = 16.0 Hz, 1H), 7.01 (d, J = 16.0 Hz, 1H), 6.86 (s, 1H), 6.5 (s, 1H), 2.61 (s, 2H), 2.48 (s, 2H), 1.00 (s, 6H); ^{13}C NMR (100 MHz, (CD$_3$)$_2$SO) δ (ppm) 170.2, 155.8, 141.4 140.0, 136.5, 133.7, 129.4, 129.0, 127.8, 122.8, 118.4, 113.8, 113.0, 108.2, 76.3, 42.2, 38.1, 31.6, 27.4; IR (KBr, cm^{-1}) 2958, 2923, 2855, 2214, 1604, 1557, 1513, 1461, 1390, 1040, 812; MALDI-TOF calcd for [M + H]$^+$, 341.177; found, 341.135.

Preparation of 3. The yellow crystals **3** was prepared according to a similar procedure of **1** using 4-(1H-1,2,4-triazol-1-yl)benzaldehyde instead of 4-(1H-imidazol-1-yl)benzaldehyde: yield 4.00 g (85%); mp 213 °C; ^{1}H NMR (400 Hz, CD$_3$Cl) δ (ppm) 8.62 (s, 1H), 8.13 (s, 1H), 7.75 (d, 2H), 7.66 (d, 2H), 7.09 (d, J = 16.0 Hz, 1H), 7.04 (d, J = 16.0 Hz, 1H), 6.89 (s, 1H), 2.62 (s, 2H), 2.48 (s, 2H), 1.10 (s, 6H); ^{13}C NMR (100 MHz, CDCl$_3$) δ (ppm) 169.0, 153.0, 152.8, 140.7, 137.4, 135.5, 135.0, 130.2, 128.8, 124.3, 120.2, 113.2, 112.5, 79.5, 43.0, 39.2, 32.0, 28.0; IR (KBr, cm^{-1}) 2959, 2922, 2870, 2216, 1607, 1564, 1519, 1460, 1399, 1049, 811; MALDI-TOF calcd for [M + H]$^+$, 342.172; found, 342.171.

Preparation of 4. The yellow crystalline solid **4** was prepared according to a similar procedure of **1** using 4-(carbazol-9-yl)-benzaldehyde instead of 4-(1H-imidazol-1-yl)benzaldehyde: yield 3.53 g (60%); mp 226 °C; ^{1}H NMR (400 Hz, CD$_3$Cl) δ (ppm) 8.16 (d, 2H), 7.75 (d, 2H), 7.63 (d, 2H), 7.47−7.40 (m, 4H), 7.31 (t, 2H), 7.12 (d, J = 16.4 Hz, 1H), 7.08 (d, J = 16.0 Hz, 1H), 6.90 (s, 1H), 2.63 (s, 2H), 2.52 (s, 2H), 1.11 (s, 6H); ^{13}C NMR (100 MHz, CDCl$_3$) δ (ppm) 169.1, 153.4, 140.4, 138.8, 135.7, 134.4, 129.7, 128.9, 127.1, 126.1, 123.9, 123.6, 120.3, 113.4, 112.6, 109.7, 79.0, 43.0 39.2, 32.0, 28.0; IR (KBr, cm^{-1}) 2957, 2925, 2868, 2218, 1598, 1566, 1511, 1450,

1398, 1227, 814; MALDI-TOF calcd for C$_{31}$H$_{25}$N$_3$, 439.205; found, 439.208.

Preparation of 5. Under nitrogen, 4-(1,4,7,10-tetraoxa-13-aza-cyclopentadecyl)benzaldehyde (0.5 g, 1.55 mmol) and 2-(3,5,5-trimethylcyclohex-2-enylidene)malononitrile (0.29 g, 1.55 mmol) were dissolved in dry acetonitrile (10 mL). Five drops of piperidine were added, and the solution was stirred at 40 °C for 8 h. After removing the solvents, the product was purified by chromatography (ethyl acetate/petroleum ether = 3/2) to give a red solid: yield 0.53 g (70%); mp 142 °C; ^{1}H NMR (400 Hz, CD$_3$Cl) δ (ppm) 7.49 (d, 2H), 7.04 (d, J = 16.0 Hz, 1H), 6.90 (d, J = 16.0 Hz, 1H), 6.80 (s, 1H), 3.80−3.64 (m, 20H), 2.59 (s, 2H), 2.46 (s, 2H), 1.08 (s, 6H); ^{13}C NMR (100 MHz, CDCl$_3$) δ (ppm) 169.2, 155.1, 148.3, 137.87, 137.83, 129.55, 124.7, 121.6, 114.2, 113.4, 112.7, 75.9, 71.1, 70.3, 70.0, 68.0, 53.2, 43.0, 39.2, 32.0, 28.0; IR (KBr, cm^{-1}) 2923, 2868, 2211, 1597, 1549, 1504, 1454, 1390, 1181, 1126, 818; HRMS (ESI-MS) calcd for [M + H]$^+$, 492.286; found, 492.285.

Preparation of Nanoaggregates. Stock ethanol solutions of the compounds with a concentration of 10^{-3} M were prepared. Aliquots of the stock solution were transferred to 10 mL volumetric flasks. After appropriate amounts of ethanol were added, water was added dropwise under vigorous stirring to furnish 5 × 10^{-5} M solutions with different water contents (0−95 vol %). The UV−vis and PL measurements of the resultant solutions were then performed immediately.

Cell Culture and Incubation. HepG2 cells were seeded in 6-well plates at a density of 2 × 10^5 cells per well and grown for 96 h. For live cell imaging, cell cultures were incubated with the chromophores (10% PBS/90% cell media) at concentrations of 40 μM and maintained at 37 °C in an atmosphere of 5% CO$_2$ and 95% air for incubation time of 2 h. The cells were then washed with PBS (3 × 3 mL per well), and 3 mL of PBS was added to each well. The cells were imaged using confocal laser scanning microscopy and water immersion lenses. Excitation energy of 458 nm was used, and the fluorescence emission was measured at 615−686 nm.

Fluorescence Imaging. HepG2 cells were luminescently imaged on a Zeiss LSM 710 META upright confocal laser scanning microscope using 40× magnification water-dipping lenses for monolayer cultures. Image data acquisition and processing was performed using Zeiss LSM Image Browser, Zeiss LSM Image Expert and Image J.

Cytotoxicity Assays in Cells. To ascertain the cytotoxic effect of the compounds' treatment over a 24 h period, the 5-dimethylthiazol-2-yl-2,5-diphenyltetrazolium bromide (MTT) assay was performed. HepG2 cells were trypsinized and plated to ~70% confluence in 96-well plates 24 h before treatment. Prior to the compounds' treatment, the DMEM was removed and replaced with fresh DMEM, and aliquots of the compound stock solutions (100 μM DMSO) were added to obtain final concentrations of 5, 10, 20, 40, and 60 μM. The treated cells were incubated for 24 h at 37 °C and under 5% CO$_2$. Subsequently, the cells were treated with 5 mg/mL MTT (40 μL/well) and incubated for an additional 4 h (37 °C, 5% CO$_2$). Then, DMEM was removed, the formazan crystals were dissolved in DMSO (150 μL/well), and the absorbance at 490 nm was recorded. The cell viability (%) was calculated according to the following equation: cell viability % = OD$_{490}$(sample)/OD$_{490}$(control) × 100, where OD$_{490}$(sample) represents the optical density of the wells treated with various concentration of the compounds and OD$_{490}$(control) represents that of the wells treated with DMEM + 10% FCS. Three independent trials were conducted, and the averages and standard deviations are reported. The reported percent cell survival values are relative to untreated control cells.

■ ASSOCIATED CONTENT

Ⓢ Supporting Information

Spectroscopic data, absorption spectra, and fluorescence of **1**−**5** in seven organic solvents. Time-resolved fluorescence curves of **1**−**5**. The changes of the integral under emission bands with different water fractions. NMR and mass spectra for

compounds **1**−**5**. This material is available free of charge via the Internet at http://pubs.acs.org.

■ AUTHOR INFORMATION

Corresponding Author

*E-mail: zhpzhp@263.net. Fax: 86-551-5107304.

Notes

The authors declare no competing financial interest.

■ REFERENCES

(1) Kim, S.; Pudavar, H. E.; Bonoiu, A.; Prasad, P. N. *Adv. Mater.* **2007**, *19*, 3791.

(2) Kim, S.; Ohulchanskyy, T. Y.; Pudavar, H. E.; Pandey, R. K.; Prasad, P. N. *J. Am. Chem. Soc.* **2007**, *129*, 2669.

(3) Yuan, W. Z.; Lu, P.; Chen, S.; Lam, J. W. Y.; Wang, Z.; Liu, Y.; Kwok, H. S.; Ma, Y.; Tang, B. Z. *Adv. Mater.* **2010**, *22*, 2159.

(4) Forrest, S. R.; Thompson, M. T. *Chem. Rev.* **2007**, *107*, 923.

(5) Thomass, S. W., III; Joly, G. D.; Swager, T. M. *Chem. Rev.* **2007**, *107*, 1339.

(6) Hong, Y. J.; Jam, W. Y.; Tang, B. Z. *Chem. Commun.* **2009**, 4332.

(7) Liu, J.; Lam, J. W. Y.; Tang, B. Z. *Chem. Rev.* **2009**, *109*, 5799.

(8) Luo, J.; Lam, J. W. Y.; Cheng, L.; Chen, H.; Qiu, C.; Kwok, H. S.; Zhan, X.; Liu, Y.; Zhu, D.; Tang, B. Z. *Chem. Commun.* **2001**, 1740.

(9) Li, Z.; Dong, Y. Q.; Lam, J. W. Y.; Sun, J.; Qin, A.; Haussler, M.; Dong, Y. P.; Sung, H. H. Y.; Williams, I. D.; Kwok, H. S.; Tang, B. Z. *Adv. Funct. Mater.* **2009**, *19*, 905.

(10) Zhao, Z. J.; Chen, S. M.; Shen, X. Y.; Mahtab, F.; Yu, Y.; Lu, P.; Lam, J. W. Y.; Kwok, H. S.; Tang, B. Z. *Chem. Commun.* **2010**, 686.

(11) Yuan, W. Z.; Chen, S. M.; Lam, J. W. Y.; Deng, C. M.; Lu, P.; Sung, H. H. Y.; Williams, I. D.; Kwok, H. S.; Zhang, Y. M.; Tang, B. Z. *Chem. Commun.* **2011**, *47*, 11216.

(12) Yu, Y.; Hong, Y.; Feng, C.; Liu, J.; Lam, J. W. Y.; Faisal, M.; Ng, K. M.; Luo, K. Q.; Tang, B. Z. *Sci. China, Ser. B: Chem.* **2009**, *52*, 15.

(13) Yu, Y.; Feng, C.; Hong, Y. N.; Liu, J. Z.; Chen, S. J.; Ng, K. M.; Luo, K. Q.; Tang, B. Z. *Adv. Mater.* **2011**, *23*, 3298.

(14) Liu, Y.; Deng, C. M.; Tang, L.; Qin, A. J.; Hu, R. R.; Sun, J. Z.; Tang, B. Z. *J. Am. Chem. Soc.* **2011**, *133*, 660.

(15) Liu, Y.; Qin, A. J.; Chen, X. J.; Shen, X. Y.; Tong, L.; Hu, R. R.; Sun, J. Z.; Tang, B. Z. *Chem.—Eur. J.* **2011**, *17*, 14736.

(16) Wang, J.; Mei, J.; Yuan, W. Z.; Lu, P.; Qin, A. J.; Sun, J. Z.; Ma, Y. G.; Tang, B. Z. *J. Mater. Chem.* **2011**, *21*, 4056.

(17) Yamaguchi, Y.; Matsubara, Y.; Ochi, T.; Wakamiya, T.; Yoshida, Z. I. *J. Am. Chem. Soc.* **2008**, *130*, 13867.

(18) Loudet, A.; Burgess, K. *Chem. Rev.* **2007**, *107*, 4891.

(19) Kabe, R.; Nakanotani, H.; Sakanoue, T.; Yahiro, M.; Adachi, C. *Adv. Mater.* **2009**, *21*, 4034.

(20) Shimizu, M.; Tatsumi, H.; Mochida, K.; Shimono, K.; Hiyama, T. *Chem.—Asian J.* **2009**, *4*, 1289.

(21) Itami, K.; Ohashi, Y.; Yoshida, J. I. *J. Org. Chem.* **2005**, *70*, 2778.

(22) Yu, Z. P.; Duan, Y. Y.; Cheng, L. H.; Han, Z. L.; Zheng, Z.; Zhou, H. P.; Wu, J. Y.; Tian, Y. P. *J. Mater. Chem.* **2012**, *22*, 16927.

(23) Hong, Y.; Lam, J. W. Y.; Tang, B. Z. *Chem. Commun.* **2009**, 4332.

(24) Yuan, W. Z.; Lu, P.; Chen, S.; Lam, J. W. Y.; Wang, Z.; Liu, Y.; Kwok, H. S.; Tang, B. Z. *Adv. Mater.* **2010**, *22*, 2159.

(25) Zhao, Z. J.; Chen, S. M.; Shen, X. Y.; Mahtab, F.; Yu, Y.; Lu, P.; Lam, J. W. Y.; Kwoka, H. S.; Tang, B. Z. *Chem. Commun.* **2010**, *46*, 686.

(26) Zhao, Z. J.; Chen, S. M.; Lam, J. W. Y.; Jim, C. K. W.; Chan, C. Y. K.; Wang, Z. M.; Lu, P.; Deng, C. M.; Kwok, H. S.; Ma, Y. G.; Tang, B. Z. *J. Phys. Chem. C* **2010**, *114*, 7963.

(27) Li, J.; Liu, D.; Hong, Z.; Tong, S.; Wang, P.; Ma, C.; Lengyel, O.; Lee, C. S.; Kwong, H. L.; Lee, S. *Chem. Mater.* **2003**, *15*, 1486.

(28) Massin, J.; Dayoub, W.; Mulatier, J. C.; Aronica, C.; Bretonnière, Y.; Andraud, C. *Chem. Mater.* **2011**, *23*, 862.

(29) Zhou, H. P.; Zhou, F. X.; Wu, P.; Zheng, Z.; Yu, Z. P.; Chen, Y. X.; Tu, Y. L.; Kong, L.; Wu, J. Y.; Tian, Y. P. *Dyes Pigm.* **2011**, *91*, 237.

(30) Wang, X. M.; Zhou, Y. F.; Yu, W. T.; Wang, C.; Fang, Q.; Jiang, M. H.; Lei, H.; Wang, H. Z. *J. Mater. Chem.* **2000**, *10*, 2698.

(31) Lemke, R. *Synthesis* **1974**, *5*, 359.

(32) Zhang, H. G.; Tao, X. T.; Chen, K. S.; Yuan, C. X.; Yan, S. N.; Jiang, M. H. *Chin. Chem. Lett.* **2011**, *22*, 647.

(33) Tong, H.; Hong, Y.; Dong, Y.; Ren, Y.; Haeussler, M.; Lam, J. W. Y.; Wong, K. S.; Tang, B. Z. *J. Phys. Chem. B* **2007**, *111*, 2000.

(34) Zhang, X. Q.; Chi, Z. G.; Zhou, X.; Liu, S. W.; Zhang, Y.; Xu, J. R. *J. Phys. Chem. C* **2012**, *116*, 23629.

(35) Zhang, X. Q.; Chi, Z. G.; Xu, B. J.; Li, H. Y.; Yang, Z. Y.; Li, X. F.; Liu, S. W.; Zhang, Y.; Xu, J. R. *Dyes Pigm.* **2011**, *89*, 56.

(36) Zhang, X. Q.; Chi, Z. G.; Xu, B. J.; Chen, C. J.; Zhou, X.; Zhang, Y.; Liu, S. W.; Xu, J. R. *J. Mater. Chem.* **2012**, *22*, 18505.

(37) Dong, S.; Li, Z.; Qin, J. *J. Phys. Chem. B* **2009**, *113*, 434.

(38) Yang, Z. Y.; Chi, Z. G.; Yu, T.; Zhang, X. Q.; Chen, M. N.; Xu, B. J.; Liu, S. W.; Zhang, Y.; Xu, J. R. *J. Mater. Chem.* **2009**, *19*, 5541.

(39) Tang, B. Z.; Geng, Y. H.; Lam, J. W. Y.; Li, B. S. *Chem. Mater.* **1999**, *11*, 1581.

(40) Lechner, M. D. *J. Serb. Chem. Soc.* **2005**, *70*, 361.

(41) Wang, F.; Bazan, G. C. *J. Am. Chem. Soc.* **2006**, *128*, 15786.

(42) Zhu, L. N.; Yang, C. L.; Qin, J. G. *Chem. Commun.* **2008**, 6303.

(43) Li, L.; Tian, Y. P.; Yang, J. X.; Sun, P. P.; Wu, J. Y.; Zhou, H. P.; Zhang, S. Y.; Jin, B. K.; Xing, X. J.; Wang, C. K.; Li, M.; Cheng, G. H.; Tang, H. H.; Huang, W. H.; Tao, X. T.; Jiang, M. H. *Chem.—Asian. J.* **2009**, *4*, 668.

(44) Strickler, S. J.; Berg, R. A. *J. Chem. Phys.* **1962**, *37*, 814.

(45) Chan, C. Y. K.; Zhao, Z. J.; Lam, J. W. Y.; Liu, J. Z.; Chen, S. M.; Lu, P.; Mahtab, F.; Chen, X. J.; Sung, H. H. Y.; Kwok, H. S.; Ma, Y. G.; Williams, I. D.; Wong, K. S.; Tang, B. Z. *Adv. Funct. Mater.* **2012**, *22*, 378.

(46) Dong, Y. Q.; Lam, J. W. Y.; Qin, A. J.; Liu, J. Z.; Li, Z.; Tang, B. Z. *Appl. Phys. Lett.* **2007**, *91*, 11111.

(47) Xu, J. L.; Liu, X. F.; Lv, J.; Zhu, M.; Huang, C. S.; Zhou, W. D.; Yin, X. D.; Liu, H. B.; Li, Y. L.; Ye, J. P. *Langmuir* **2008**, *24*, 8.

(48) Shen, X. Y.; Yuan, W. Z.; Liu, Y.; Zhao, Q. L.; Lu, P.; Ma, Y. G.; Williams, I. D.; Qin, A. J.; Sun, J. Z.; Tang, B. Z. *J. Phys. Chem. C* **2012**, *116*, 10541.

(49) Li, Y. X.; Chen, Z.; Cui, Y.; Xia, G. M.; Yang, X. F. *J. Phys. Chem. C* **2012**, *116*, 6401.

(50) Ju, H. D.; Tao, X. T.; Wan, Y.; Shi, J. H.; Yang, J. X.; Xin, Q.; Zou, D. C.; Jiang, M. H. *Chem. Phys. Lett.* **2006**, *432*, 321.

(51) Zheng, Z.; Zhang, Q.; Yu, Z. P.; Yang, M. D.; Zhou, H. P.; Wu, J. Y.; Tian, Y. P. *J. Mater. Chem. C* **2013**, *1*, 822.

(52) Zhang, H. G.; Tao, X. T.; Chen, K. S.; Yuan, C. X.; Jiang, M. H. *Synth. Met.* **2011**, *161*, 354.